Journal of Geochemical Exploration 263 (2024) 107510

Contents lists available at ScienceDirect

Journal of Geochemical Exploration

journal homepage: www.elsevier.com/locate/gexplo

Inferring arsenic anomalies indirectly using airborne hyperspectral imaging – Implication for gold prospecting along the Rise and Shine Shear Zone in New Zealand

Rupsa Chakraborty [a,*], Gabor Kereszturi [a], Reddy Pullanagari [b], Dave Craw [c], Patricia Durance [d], Salman Ashraf [e]

[a] Geosciences, School of Agriculture and Environment, Massey University, Palmerston North, New Zealand
[b] MAF Digital Lab, School of Food and Advanced Technology, Massey University, Palmerston North, New Zealand
[c] Geology Department, University of Otago, Dunedin, New Zealand
[d] BHP Billiton, Perth, Western Australia, Australia
[e] GNS Science, Avalon, Lower Hutt, New Zealand

ARTICLE INFO

Keywords:
Hyperspectral imaging
Band selection
OTVCA
Gold mineralisation
Arsenic
Classification

ABSTRACT

Well-exposed mineral deposits are scarce at a global level and presently potential mineral-rich sites are underlying vegetation cover and topsoil, which are suboptimal for direct remote sensing based exploration techniques. This study aims to implement an indirect approach to arsenic (As) distribution mapping using the surface manifestations of the subsurface geology and link it to the known gold mineralisation in the study area. Rise and Shine Shear Zone (RSSZ) in New Zealand is broadly a part of the Otago schist hosting lower to upper green-schist facies rocks manifesting mesothermal gold mineralisation. The area has several surficial geological imprints separating mineralised and non-mineralised zones, but these are dominated by topographic ruggedness, soil moisture and vegetation (mainly grass/tussock) spectra in the hyperspectral data. Initially, a band selection using Recursive Feature Elimination (RFE) was executed. The bands generated were tallied with the field and geological understanding of the area. The resultant 85 bands were then further put through Orthogonal Total Variation Component Analysis (OTVCA) to concise the information in 10 bands. OTVCA output was then classified using Random Forest classifier to map three levels of As concentration (<20 ppm, between 20 and 100 ppm and >100 ppm). The potentially high As concentration zones are likely to be related to the gold mineralisation. The geology of the area correlates with soil exposure which is captured by the classification in some parts, this increases the accuracy but also makes the classification analysis challenging.

1. Introduction

Hyperspectral imaging measures reflected and emitted energy from the Earth's surface at hundreds of contiguous spectral bands. Hyperspectral data can span over multiple parts of the electromagnetic spectrum, including the; visible (VIS; 400–700 nm), near-infrared (NIR; 700–1200 nm), shortwave infrared (SWIR; 1000–2500 nm), mid-wave infrared (MWIR; 3000–7000 nm), and longwave infrared or thermal domains (LWIR; 7000–13,000 nm) (van Ruitenbeek et al., 2005; Kriesel et al., 2011; Kruse et al., 2012; Ullah et al., 2012; Notesco et al., 2014b; van der Meer, 2018; Simpson and Christie, 2019; Kereszturi et al., 2020; Laukamp et al., 2021b; Tripathi and Garg, 2021). Hyperspectral data can deliver spectrally 'rich' information due to its narrow and contiguous spectral band design. However, it comes at an expense of higher dimensionality and increased noise, such as instrumental and atmospheric among others, compared to broadband multispectral imaging (Mielke et al., 2014; Ghamisi et al., 2017b; Laukamp et al., 2021b). Overcoming the complexity of data processing has led to many applications, including agriculture, planetary studies (Kusuma et al., 2012; Chauhan et al., 2015), ecology, water/coastal studies, geology (van der Meer et al., 2018a; van der Meer, 2018), geothermal exploration (Rodriguez-Gomez et al., 2021), and soil science (Wei et al., 2020).

Mineral exploration can benefit from hyperspectral remote sensing due to its capacity to spatially map minerals by measuring absorption

* Corresponding author.
E-mail address: r.chakraborty@hzdr.de (R. Chakraborty).

https://doi.org/10.1016/j.gexplo.2024.107510
Received 4 August 2022; Received in revised form 6 March 2024; Accepted 20 May 2024
Available online 22 May 2024

due to molecular bonds and vibrational processes. Furthermore, reconnaissance survey using airborne and satellite-based hyperspectral data is also a fast and cheap method for vectoring in mineralised zones (Cloutier et al., 2021). For instance, the SWIR region has the potential to detect phyllosilicates, sulphates, carbonates, chlorites and many other alteration minerals (Hunt, 1982; van der Meer and Bakker, 1997; Sabins, 1999; Clark et al., 2003; van Ruitenbeek et al., 2014; van der Meer, 2018). Previous studies have been utilising hyperspectral imaging for mapping indicator minerals using 'direct' information, such as wavelength position and depth (Kruse, 1998; van der Meer, 2001; Bishop, 2005; Kruse, 2007; Pour and Hashim, 2011; Notesco et al., 2014a; Kereszturi et al., 2018). In a standard hyperspectral imaging mapping workflow, the reflectance data is initially put through minimum noise fraction (MNF) for dimensionality reduction. MNF includes two levels of rotation, the first separates the noise from the information and in the second rotation the noise-whitened data is further transformed to

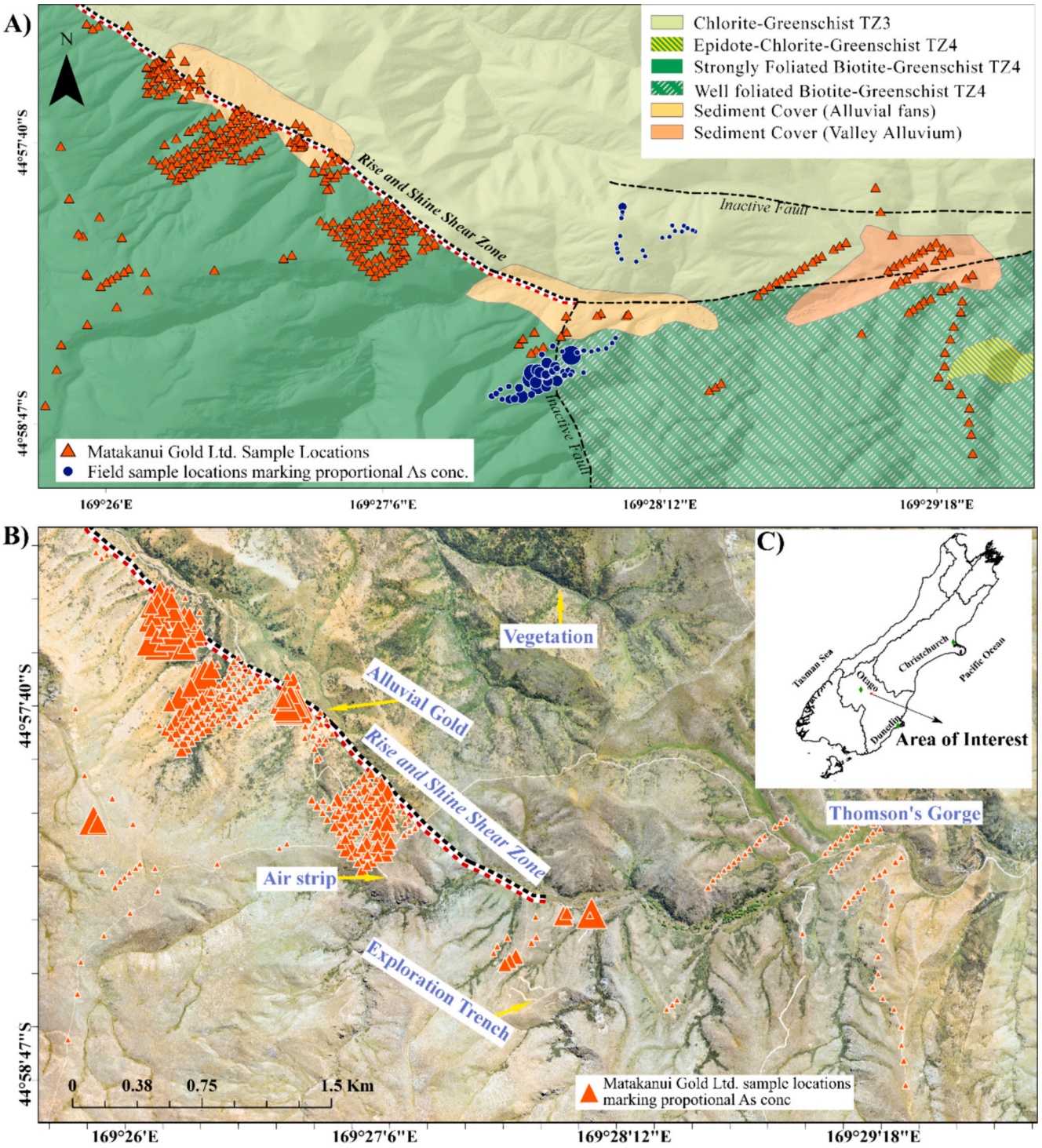

Fig. 1. A) Simplified geological map of the Upper Thomson Gorge, overlaid by the sampling locations (blue dots) and geochemical vectoring data provided by Matakanui Gold Ltd. (orange triangles). B) RGB orthophoto of the same area, representing the ruggedness of the terrain and the grass/tussock cover. C) On a map of South Island, New Zealand, the key places and the study area are marked for a broader idea of the location. (For interpretation of the references to colour in this figure legend, the reader is referred to the web version of this article.)

capture the maximum variance in the data (Wu et al., 2013). This is followed by identifying the pure pixels indices that are then used for selecting the endmembers to form the training subset. These endmembers are finally used in mapping algorithms for generating abundance maps (Clark et al., 1993; Boardman et al., 1995; Kruse et al., 2003; Kruse, 2007; Kruse et al., 2012). This is a powerful approach when the targeted exploration site is well-exposed, such as the famous Cuprite dataset (van der Meer and Bakker, 1997; Swayze et al., 2014). However, Cuprite and other similar sites with well-exposed exploration targets (i.e., none to sparse vegetation, thin regolith cover) represent a minor percentage of the current mineral prospect globally, demanding new approaches that can handle partial to full vegetation cover.

The opportunity can rise to capitalise on the complexity of the hyperspectral data by integrating advanced statistical methods, such as machine learning (Ghamisi et al., 2017b). The advent of machine learning in hyperspectral remote sensing has brought many effective algorithms (e.g., random forest, support vector machine, neural networks, advanced spectral unmixing methods), to tackle the complexity of the data and extended many solutions to the inherent challenges (Cheng and Sun, 2016; Ghamisi et al., 2017a; Pullanagari et al., 2017a; Naik et al., 2021; Rodriguez-Gomez et al., 2021). One of the major advances in the recent hyperspectral sensors is the finer spectral resolution which leads to hundreds and even thousands of bands/variables, increasing computation demand. Thus, variable selection methods, such as least absolute shrinkage and selection operator (LASSO), stepwise selection, and recursive feature elimination (RFE) have been utilised to improve computation time, costs, and applicability of the resultant statistics (Guyon and Elisseeff, 2003; Zou, 2006; Paul et al., 2008; Kursa et al., 2010; Zhou et al., 2014; Han et al., 2016; Demarchi et al., 2020; Lotfollahi et al., 2020).

The present study aims to explore the information captured by hyperspectral data for mineral exploration using a mineral prospect from New Zealand with partial to full vegetation cover (i.e., 'less optimal' for hyperspectral data). This study, therefore, employs an alternative approach that can build on indirect interference to locate mineral resources underground. This study is based on the Rise and Shine shear zone (RSSZ) in South Island, New Zealand (Fig. 1A), which hosts a mesothermal gold mineralisation in the upper green-schist facies rock (Craw and MacKenzie, 2007; MacKenzie and Craw, 2007). It is a highly rugged terrain showing a diverse range of exposed soil (5–80 %), and sparse grass and tussock vegetation cover (Fig. 1B). Using a 2 m spatial resolution airborne hyperspectral data, this study allows us to depict the complexities of the reflectance signals, including exposure fraction and influences of vegetation while developing a new screening method to locate underground gold mineralisation. Utilising certain surface manifestations (Table 1) caused by leaching of arsenopyrite and scorodite which pathfinder minerals to gold in the RSSZ as a proxy to map arsenic (As) distribution in the region.

2. Geological settings

The RSSZ is part of the Otago Schist and is exposed as a ~50–100 m wide zone that strikes northwest across the Dunstan Range. The schists were pervasively recrystallised and foliated during metamorphism and now consist of highly segregated quartz-albite and chlorite-phengitic muscovite laminations at the centimetre scale. The shear zone is hosted in upper greenschist facies schists that have been juxtaposed against lower greenschist facies schist. The shear zone dips gently (~15–20°) to the northeast in the footwall of the Thomson's Gorge Fault, a post-mineralisation normal fault (MacKenzie and Craw, 2007). Fresh mineralised schist contains disseminated arsenopyrite in foliation-parallel shears and breccias, and gold is closely associated with this arsenopyrite (Fig. 1) (Mortimer, 2000; Craw et al., 2005; Christie, 2016; Cudby et al., 2021). Metamorphic chlorite was extensively altered to hydrothermal Fe-Mg-Ca carbonate (ankerite) during mineralisation. Oxidation of the mineralised zone has caused abundant ferric oxyhydroxide to form during the decomposition of arsenopyrite and ankerite. The ferric oxyhydroxide has variable amounts of adsorbed and intergrown As, and both Fe and As have been extensively remobilised onto fractures and foliation surfaces.

Table 1
Theoretical parameters differentiating non-mineralised from mineralised and the corresponding hyperspectral signals driving the study. (Veg-vegetation).

Attribute	Non-mineralised	Weakly mineralised	Strongly mineralised
Shear zone features at the surface			
Gold	Below detection	<0.5 ppm; rare veg	>1 ppm; rare veg
Arsenic	<30 ppm	>50 ppm	>1000 ppm
Shear zone trace	Sharp boundary to NE (Thomsons Gorge Fault) Diffuse boundary to SW	Strong feature, NW strike, 20 m wide at the surface	Strong feature, NW strike, wider surface zone, to 100 m
Outcrop structure	Foliation dominated	Foliation and shears	Foliation and shears
Carbonate	Minor calcite	Minor calcite, ankerite	Abundant ankerite
Hydrothermal alteration	No alteration mienrals	Alteration of chlorite to ankerite	Ankerite completely replaces chlorite
Kaolinite	Minor alterations from the Cenozoic era	Minor from Cenozoic alteration; some hydrothermal	Minor Cenozoic alteration; abundant hydrothermal alteration
Ferric oxyhydroxide	Minor alterations from the Cenozoic era	Abundant from sulphides and ankerite	Abundant from sulphides and ankerite
Surface	Outcrops, colluvium	Abundant scree from sheared rock	Abundant scree from sheared rock
Expected hyperspectral signals at the surface			
Surface features	Mostly vegetated	Abundant bare ground	Abundant bare ground
Chlorite (~2250 nm)	Strong Mg-OH signal	Weak Mg-OH signal	No Mg-OH signal
Kaolinite (2200 and 2300 nm)	Weak Al-OH signal	Moderate Al-OH signal	Strong Al-OH signal
Ferric oxyhydroxide (450–550 nm)	Weak Fe-OH signal	Moderate Fe-OH signal	Strong Fe-OH signal
Carbonate (2320 nm)	Weak CO_3 signal	Moderate CO_3 signal	Moderate CO_3 signal

Gold occurrence here is often signalled by elevated As concentration due to the supergene breakdown of arsenopyrite, forming As-rich halos around the ore bodies. The Ca-poor ankerite alteration phase is also a characteristic indicator mineral for gold mineralisation along the RSSZ. The precipitation of ankerite through the decomposition of metamorphic chlorite released Fe, triggering the formation of arsenopyrite and other sulphide minerals. This leads to sulphur depletion in the hydrothermal fluid destabilising the Au—S complexes and causing disseminated gold deposition (MacKenzie et al., 2006; Craw and MacKenzie, 2007).

The gold mineralisation here sits at a depth of 5–10 km and the proximal mineralisation halo extends upto ~100 m (Cox et al., 2006; Mortensen et al., 2010). The mineralised schist is often overlain by unconsolidated Quaternary sediments. These loose sediments are easily eroded by surficial processes bringing the ore bodies closer to the surface. The erosion of the overlaid sediments makes the mineralised shear zone prone to oxidation caused by groundwater and atmosphere along with supergene enrichment (Craw, 1994; Craw et al., 2015). The sulphide-bearing minerals from the mineralised schist (e.g., pyrite and arsenopyrite) at near-surface atmospheric conditions are metastable and can easily decompose by oxidation forming metal hydroxides (e.g., iron-

hydroxide formed by the transformation of arsenopyrite). Near-surface oxidation and weathering further result in an environment which facilitates physical and chemical mobility for gold and associated metal hydroxides (Blake et al., 2019; Beyer et al., 2021; Cudby et al., 2021). Gold in its free form is adsorbed by these metal hydroxides to form gold nuggets, which are subjected to surficial processes. This brings gold and its associated minerals (such as As) close to surface (<25 cm depth) making an impact in the surface cover and soil.

The soil along the RSSZ is strongly controlled by the ore-bearing schistose parental material, which is in turn controlling its bulk soil geochemistry and weathering (Martin et al., 2016). Soil overlying biotite, chlorite-rich green-schist facies rocks show elevated As concentration in both A (0–30 cm) and B (50–70 cm) horizons, while on the contrary, soil developed on lower-grade metamorphic basement rocks show baseline concentrations. Recently, soils of Southland and Otago have been analysed by Inductively Coupled Plasma Mass Spectrometry (ICPMS) and XRF for multiple elements, including As (Martin et al., 2016; Martin et al., 2018). The sampling has been carried out at a regular 8 km grid spacing that can provide an adequate As baseline information for the RSSZ.

3. Materials and methods

3.1. Field campaigns, sampling, and rock analysis

The field sampling sites were selected based on As and gold concentration through a pXRF soil analysis dataset previously collected by the Matakanui Gold Ltd. and the geological knowledge of the area (Cox et al., 2006; Craw and MacKenzie, 2007). Following this data and field accessibility, the sampling was targeted to incorporate the potential zones of mineralised and non-mineralised zones. In total 63 soil samples were collected, covering a range of exposure conditions (Fig. 2). The soil exposure percentage was quantified based on 100 random point counts from near-nadir hand-held digital photos (Fig. 2A-C). The details of all 63 sample locations are provided in the Supplementary Data (Table S1).

The field soil samples were collected from A-depth, 5–20 cm immediately beneath the vegetation cover (Fig. 2 D—F). The rock fragments encountered typically at the interface of the soil and rock were also sampled. A total of 42 soil samples were collected from the mineralised zone and the remaining 21 samples were collected from the non-mineralised zone for training purposes. This data was used for band selection and in the "direct" mapping workflow.

An additional 309 samples out of an extensive dataset of 1500 samples were also used. This database was developed through multi-year field campaigns and analysis using pXRF on the surface soil for As by Matakanui Gold Ltd. (Fig. 1). These 309 samples were grouped into three classes to represent the previously established geochemical baseline (i.e., <20 ppm; Martin et al. (2016)), medium (20–100 ppm) and high As (>100 pm) that is indicative of underlying gold deposits.

A selected range of rock samples from both the mineralised and non-mineralised regions along with a scorodite-bearing schist rock sampled by Cudby et al. (2021) were examined using Scanning Electron Microscope (SEM) which was equipped with energy-dispersive X-ray spectroscopy (EDS), for detailed mineralogical and compositional analysis. Thick (~0.6 to ~0.8 mm) sections of the rock were mounted on glass slides. The thick sections were then carbon coated and imaged using ThermoFisher Scientific™ FEI Quanta 200 Environmental Scanning Electron Microscope. The SEM was operated in Back-scattered electron (BSE) mode under an accelerating voltage of 20 kV, at the wondering distance of 10 mm. The EDS on the same thick section was operated at an accelerating voltage of 25 kV.

3.2. Airborne hyperspectral surveys and data processing

The airborne hyperspectral data was captured by a push-broom AisaFENIX sensor, operated jointly with a Nikon D810 digital single-lens reflex camera. The airborne survey was designed to capture hyperspectral data at a 2 m spatial resolution with 30 % side overlap. The airborne experiment was carried out at local noon on the 11th of February 2020. The details of the sensor specifications are tabulated in Table 2 and pre-processing workflow can be found in Chakraborty et al. (2022).

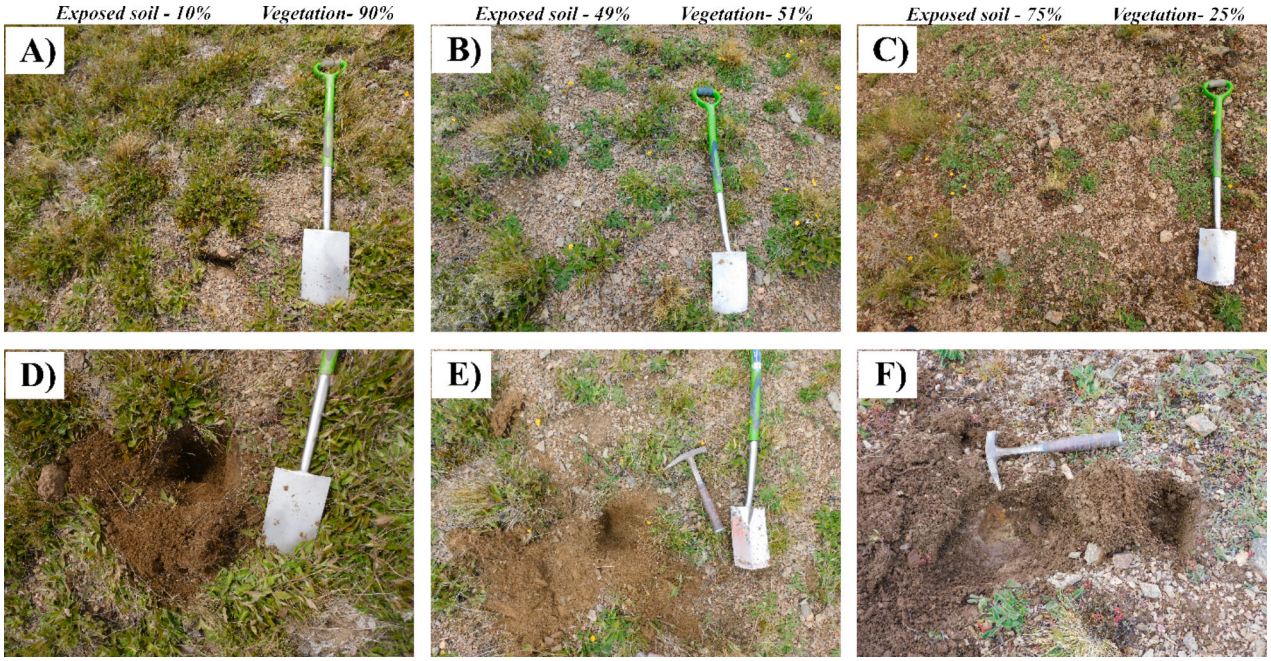

Fig. 2. A range of soil exposures, varying approximately from 10 to 80 % at sampling sites RSS59, RSS42 and RSS7. The spade and hammer are ca. 100 cm and 30 cm long, respectively.

Table 2
AisaFENIX specifications.

	VNIR	SWIR
Field of View	32.2°	
Instantaneous Field of View	0.084°	
Full-Width-Half-Maximum	3.2–12.2 nm	
Spectral Bandwidth	~3.3 nm	~5.7 nm
Number of Bands	177	272
Spectral Range	0.3773–0.9775 μm	0.9831–2.4918 μm

3.2.1. Reflectance spectroscopy and pXRF analysis

The 63 field soil samples were oven dried at ~65 °C for about two days. The samples were then coarsely ground and sieved to a 2 mm grain size before acquiring VIS-SWIR reflectance using an ASD FieldSpec 4 High-Resolution spectrometer at Massey University. This instrument collects light reflectance from 350 nm to 2500 nm with a spectral interval of 1 nm. A small portion of the soil sample was transferred on a petri dish with a black background, the data was then obtained by direct spot measurements in 5 different spots, using a high-intensity contact probe. Before each measurement, white reference calibration was performed with a Spectralon® reference, to ensure optimised and weighted reflectance values across the spectrum. The individual spot measurements were and average of 10 acquisitions with an iteration time of 17 μs which were then splice corrected before further analysis.

The 63 field soil samples were also analysed to quantify As concentration using an Olympus Innov-X Delta series portable X-Ray Fluorescence (pXRF) machine, at GNS Science, Lower Hutt. The pXRF was calibrated before-, midway-, and after the soil measurements using two standardised calibration samples provided by Olympus (Durance et al., 2014).

3.3. Absorption depth mapping and band ratios – "Direct" methods

In this study, the wavelength mapper (van der Meer et al., 2018b) was used to map absorption features through partial exposure. Wavelength mapper calculates the location and depth of the maximum absorption feature of the target material (van der Meer et al., 2018b). The deeper the absorption feature typically means more abundant the target material (van Ruitenbeek et al., 2014; Dalm et al., 2017; van der Meer et al., 2018b; van der Meer, 2018). Here, we used two wavelength regions: 450–550 nm and 2250–2360 nm to map the Fe-OH and the chlorite absorption depth, respectively. The difference in the absorption depth at these ranges between mineralised and non-mineralised samples were validated by laboratory hyperspectral data.

3.4. Proposed Workflow- "indirect" method

We have implemented a novel workflow to classify the surface manifestations of arsenopyrite-bearing host rock and to eventually locate As anomalies that can be used for gold prospecting (Fig. 3). In the hyperspectral data processing, the first two and the last three bands were excluded from analysis due to their extremely high sensor-induced noise proportion, reducing the total number of bands to 444. This data was smoothed by the Savitzky-Golay filter (filter window of 3 bands and degree of a polynomial of 2) and continuum removed (Pullanagari et al., 2017b; Rathod et al., 2018; Chakraborty et al., 2022). The hyperspectral data was further masked by using a normalised difference vegetation index (NDVI >0.6), and also areas within 4 m around dirt/gravel roads. The buffer of 4 m was chosen to maximise the number of training data which was 309 out of 510 total sample population.

Band selection was carried out using RFE on airborne hyperspectral data using random forest as the base algorithm in a regression capacity and the As relative concentration indicated by counts at 10.54 keV which is the As k-alpha peak, from the pXRF spectra of the 63 laboratory-based samples (Fig. 4). RFE generates a relevant set of important bands to map the corresponding surficial differences in the mineralised and non-mineralised zones and eventually vectoring towards potential As anomalies. RFE is based on a feature ranking technique. It initiates from a complete set of predictor variables and discards the least relevant variables one by one by ranking them according to their importance (Zhou et al., 2014; Pullanagari et al., 2018; Demarchi et al., 2020). RFE was run using the R program in the caret package with

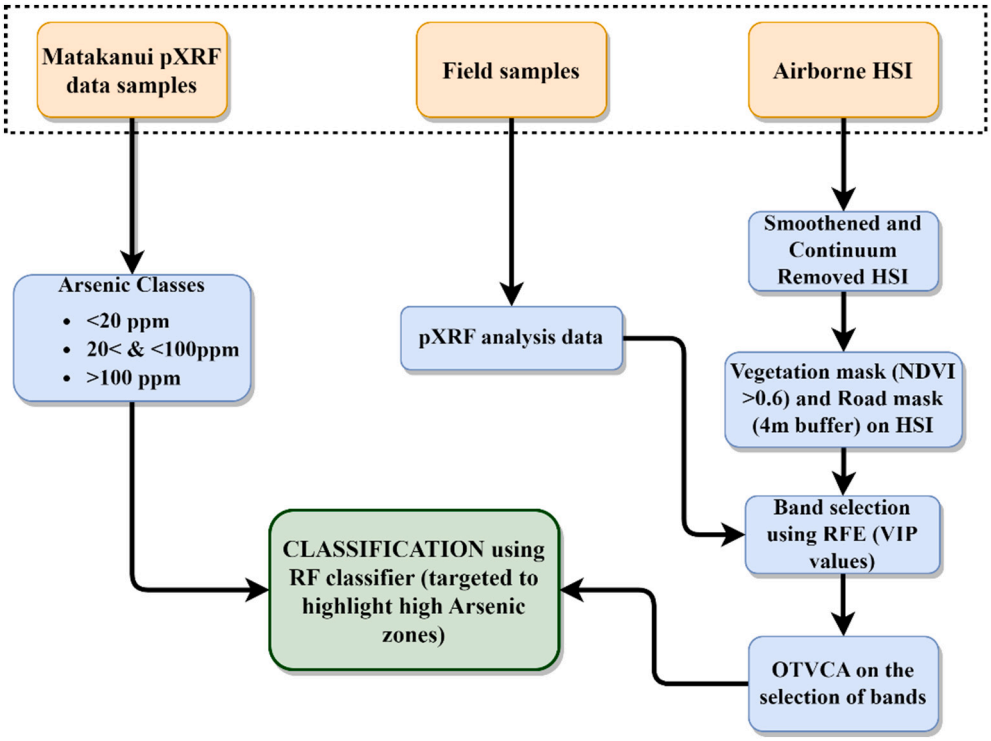

Fig. 3. Proposed workflow for potential As zonation.

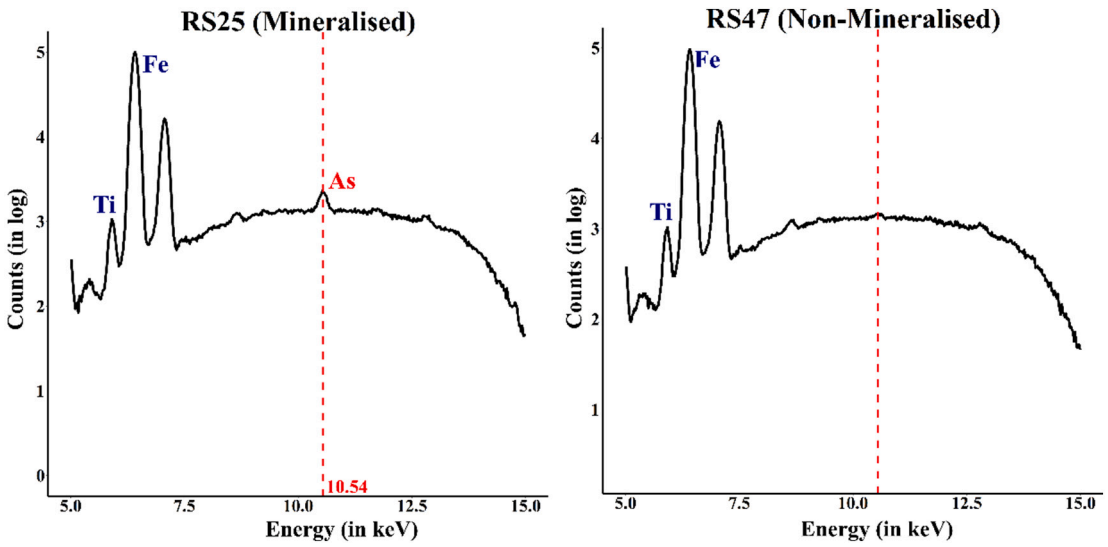

Fig. 4. A and B are pXRF spectra of a representative mineralised and non-mineralised field sample. The mineralised samples show characteristic As peak at 10.54 keV.

LOOCV cross-validation and the RF base algorithm was run on random hyperparameter search. The selected bands using the RFE were further validated using a Pearson-type correlation coefficient that was calculated between the counts received at 10.54 keV from the pXRF spectra and the normalised continuum removed from the laboratory-based VIS-SWIR reflectance spectra.

The RFE-selected wavelengths (85 bands) and the corresponding bands in the airborne hyperspectral data were further reduced using an unsupervised orthogonal total variation component analysis (OTVCA) for dimension reduction. OTVCA uses orthogonal feature transformation to find the maximum variance while it also considers the spatial information of the neighbouring pixels using a total variation penalty factor (Fauvel et al., 2012; Rasti et al., 2016; Ghamisi et al., 2017b). OTVCA thus potentially conserves spectral and spatial information from a hyperspectral image better than the most commonly used PCA or Minimum Noise Fraction (Rasti et al., 2016; Rasti et al., 2020) (in Supplementary data Fig. S1). OTVCA reduces the dimension by optimising the cost function to find the best representation of the hyperspectral dataset in a lower-dimensional feature space. The output is also optimised for spatial smoothness by using a total variation regularisation. The total variation regularisation enables piecewise smoothness on the initially extracted features which secure the pixel neighbourhood information that is crucial for further classification (Rasti et al., 2016). To prevent OTVCA from over-smoothing the hyperspectral data, the selection of the TV regularisation tuning parameter (λ) is set to 1 % of the maximum reflectance of the area of interest (Rasti et al., 2020). In this study, it was calculated based on the reflectance values of the ground sampling points. The maximum continuum-removed reflectance value was 1 and the λ was set at 0.01. The OTVCA was operated in MATLAB™. A total of 10 components were extracted using OTVCA. This number was decided visually where beyond 10 all the consecutive components showed only noise.

The OTVCA-transformed hyperspectral data was used as a predictor variable or features while the grouped Matakanui Gold Ltd. dataset into low, medium and high As concentration classes as target classes, implemented in a random forest classifier. The random forest classifier was chosen due to its ability to deal with multicollinearity and random distribution of variables. Random forest is known for its lack of ability to extrapolate beyond the input data range (Hengl et al., 2018). However, given the training data encompasses 0 (background) to 1000 ppm (extremely high), this limitation has a negligible impact on our results.

Random forest generates decision trees using the subset of training data and variables. Each of the decision trees grows independently to a maximum extent using the bagging method (Breiman, 2001; Pullanagari et al., 2017a). Each tree casts a vote for the most popular class at the input subset, and the final output of the classifier is based on a majority vote of the trees (Gislason et al., 2006). In this study the total number of trees (ntree) was set at 500, to provide enough generalisation of the model, which generates the trees with high variance and minimal bias (Belgiu and Drăguţ, 2016). The number of splits at each node (mtry) was selected using a sequential expand grid from 1 to 100 and the default random search was used. The model was validated using Leave one out cross-validation (LOOCV). The classifier's performance was assessed based on overall accuracy, along with the user's, producer's accuracy and F1 accuracy (Liu et al., 2007). This was considered a suitable measure as relative differences and accuracies among the classes have been analysed for the final interpretation.

4. Results and interpretations

4.1. Host rock analysis

The SEM-BSE analysis was executed on selected rock samples based on analysis of VIS-SWIR reflectance spectra and some from active exploration sites. The scorodite and arsenopyrite-bearing Otago schist rock, sampled by Cudby et al. (2021) marks the most confined halo of the gold mineralisation in the RSSZ. This rock type falls in the upper green-schist facies and is depleted of white mica. The scorodite-bearing schist is the parent host rock for gold in the RSSZ setting (Fig. 5a) (Craw and Lilly, 2016; Craw, 2017; Cudby et al., 2021). The surface indicator of this confined mineral phase is ferric oxyhydroxide containing adsorbed As. This is generally amorphous and has variable compositions with Fe/As>1 (Fig. 5b) (Cudby et al., 2021). The rock sample (Fig. 5b) is derived from RSS25 location which shows patches of elevated As concentration.

4.2. Direct absorption mapping and classification

The ground samples show a range of abundance and depletion of ferric hydroxide and chlorite detected at 450–550 nm and at 2250–2360 nm, respectively. The deeper the absorption features the higher the mineral abundance (Clark, 1999; van der Meer et al., 2018b). The

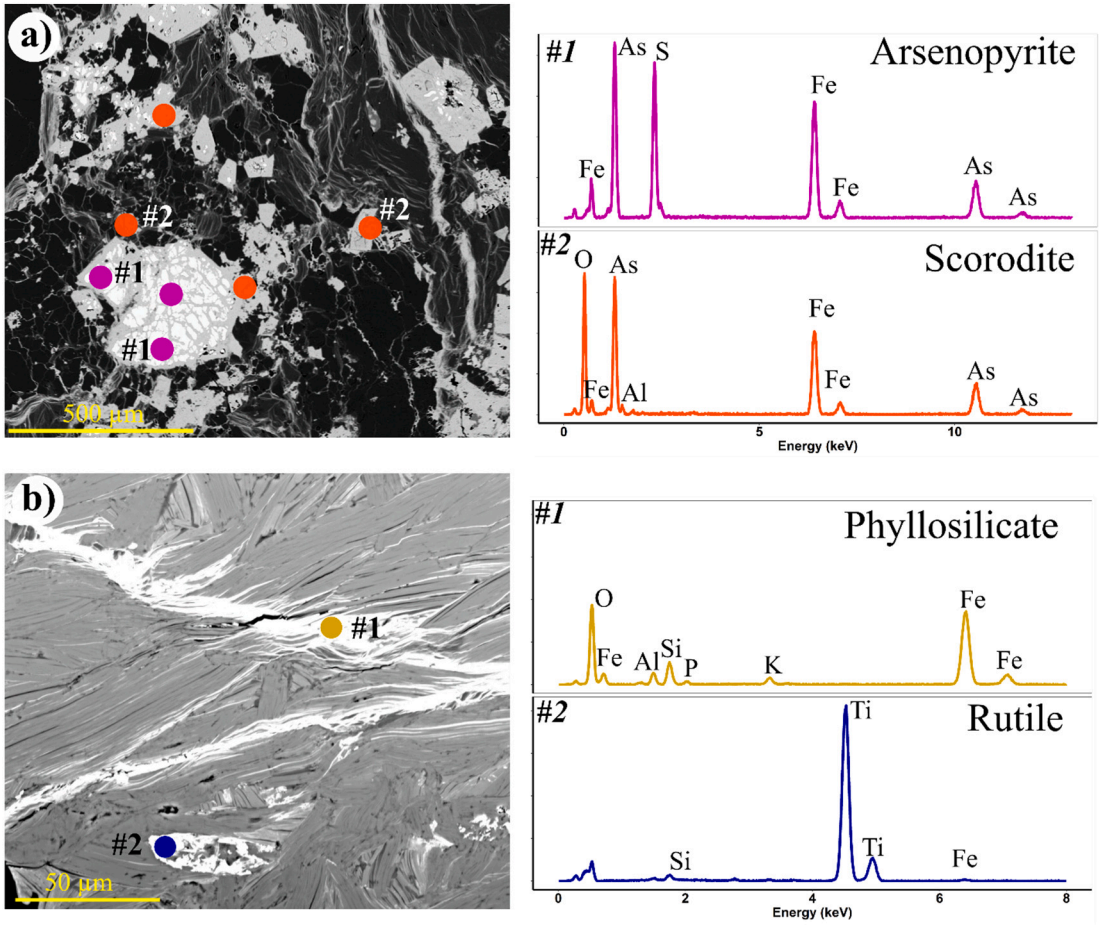

Fig. 5. SEM-BSE images (left column) and EDS spectra (right column) of representative scorodite bearing schist, mineralised upper green-schist, and non-mineralised lower green-schist samples (top to bottom). a) The bigger scorodite (#2) grains host smaller brecciated arsenopyrite (#1). b) The mineralised rock sample exhibits an elevated concentration of secondary ferric oxyhydroxide mobilised along shears and schist foliation (#1) and hydrothermal rutile (#2). (For interpretation of the references to colour in this figure legend, the reader is referred to the web version of this article.)

absorption depth mapping results using airborne hyperspectral image were here thresholded to provide individualised distribution of ferric hydroxide and chlorite minerals (Fig. 6). The band depth threshold was decided by analysing the band depth distribution along with visual interpretation. In order to mark chlorite depletion, band depth < 0.06 was chosen while band depth > 0.5 was considered for ferric hydroxide (Fig. 6). The depleted chlorite area covers an area of 1.45 km^2 and the ferric hydroxide abundant area covers an area of 3.56 km^2. Theoretically both strong ferric hydroxide absorption and chlorite depletion can indicate underlying mineralisation in the upper greenschist facies rocks based on Fig. 6, both indicator minerals seem to show some interference in topographic signalas with the nimeraligy and soil chemistry (Fig. S3B).

The map distribution represents little value for mineral prospecting. The absorption in the SWIR range targeted to map the Fe-bearing chlorite depletion also has overlapping absorption wavelengths with the clay minerals present there such as illite and smectite (Abweny et al., 2016). This renders the direct abundance mapping of chlorite even more ineffective (Fig. S3A) in such a scenario. The strong signal difference in mineral phases at a subsurface level dissipates when it comes to surface mapping where more prominent surficial parameters such as vegetation cover, soil moisture, water solubility and distribution mask the well-defined mineralogical boundaries.

The absorption feature shape shows only weak differences between mineralised and non-mineralised samples of chlorite at both laboratory-based (at ~2347 nm) and airborne (at ~2344 nm) data (Fig. 7A, B, C). The subtle change in depth for the chlorite-related absorption feature can indirectly indicate potential As-enrichment zones and consequent chlorite depletion in the host rock (Craw and MacKenzie, 2007). However, the signature chlorite absorption at ~2250 nm is only present in the laboratory spectra, but it shows no clear difference in depth between the mineralised and non-mineralised zones (Fig. 7A). In contrast, the second chlorite absorption at ~2340 nm shows a clear separation between mineralised and non-mineralised zones at the laboratory scale (Fig. 7A). This systematic is captured much less clearly by the airborne data due to decreased signal-to-noise ratio and spectral missing within the footprint of a pixel. Furthermore, there are a few absorption features scattered throughout the range (2240–2360 nm) which can be, related to both chlorite-group minerals and/or carbonate-bearing minerals (such as calcite and ankerite) based on absorption depth positions. The carbonate mineral at RSSZ changes from calcite to ankerite (MacKenzie et al., 2006; Craw and MacKenzie, 2007; Craw et al., 2007) from non-mineralised lower greenschist to mineralised upper greenschist rocks, which makes the carbonate absorption feature at ~2300 nm to be "constant". This renders carbonate abundance inadequate for differentiating mineralised from non-mineralised.

The ferric hydroxide-related absorption shows no related demarcation in absorption depth at the laboratory-scale, while only showing a vague trend at the airborne scales. Despite being ubiquitous along the RSSZ and characterised by a very strong spectral response, the ferric hydroxide absorption feature at 450–600 nm appears to be of limited use for vectoring for gold. The lack of trend can further be linked to

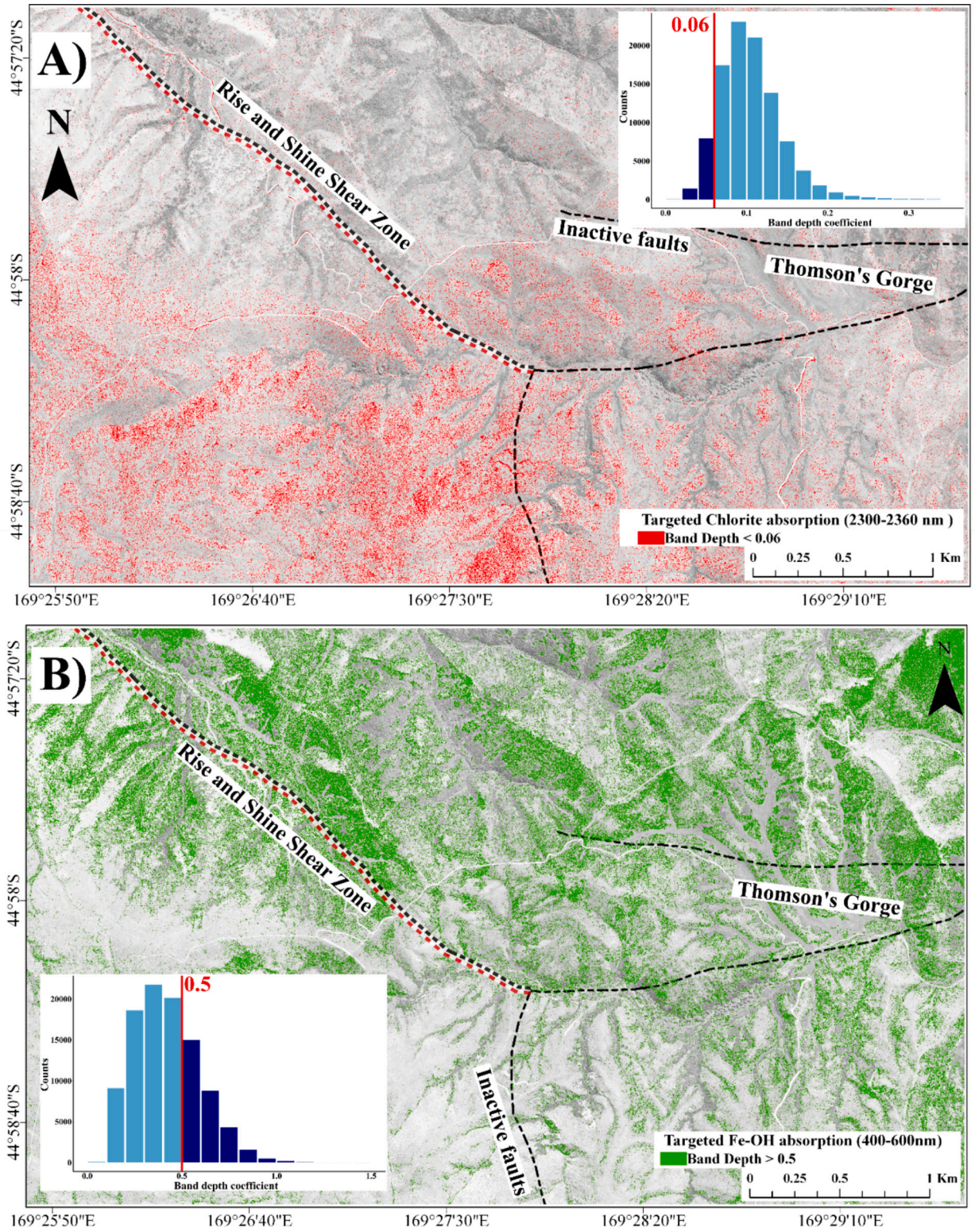

Fig. 6. Band depth mapping results targeting A) chlorite and B) ferric hydroxide absorption feature. Highlighted areas in both maps correspond to the mineralised area returned by the band depth mapping approach. The underlying geological units are shown in Fig. 1A.

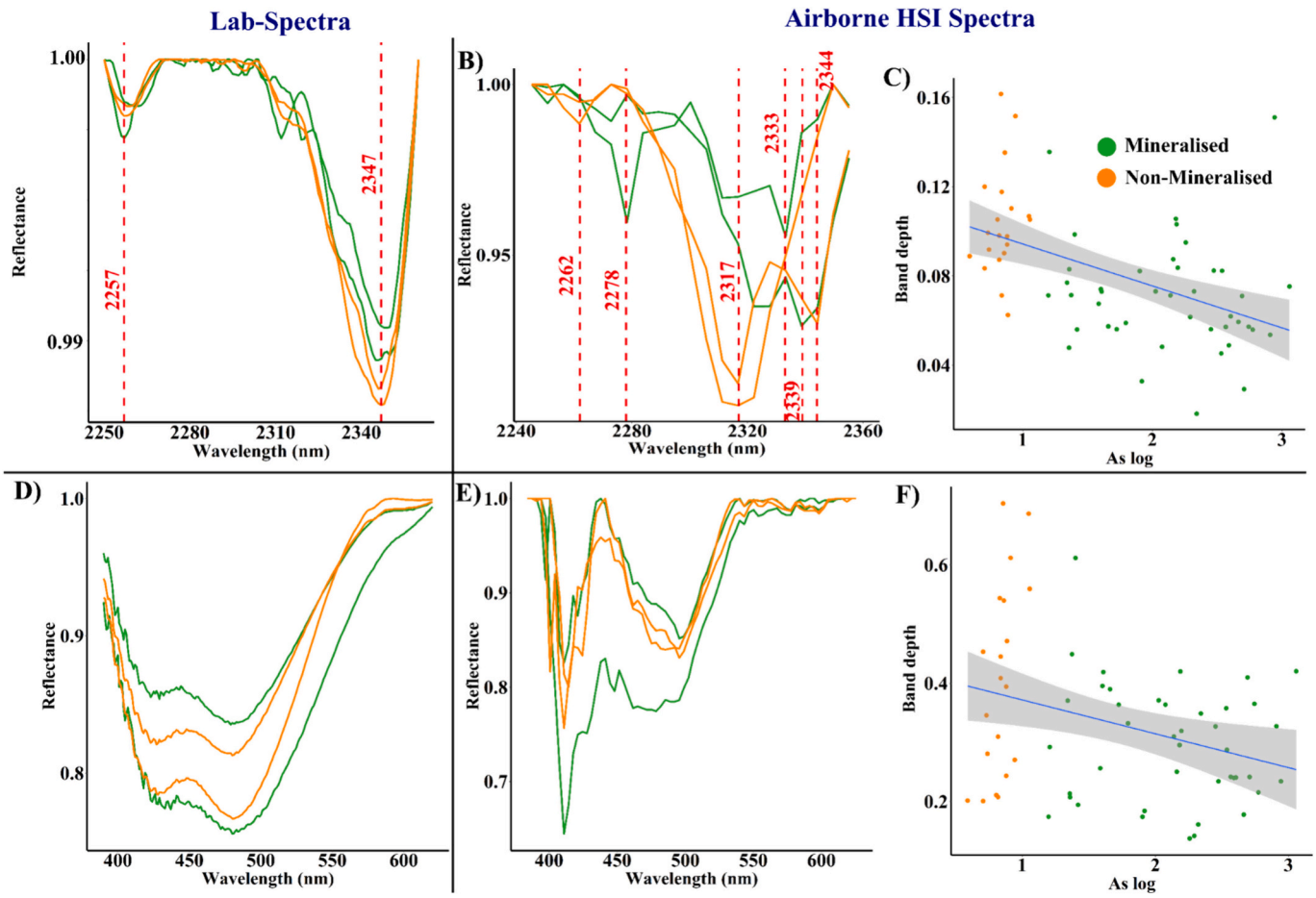

Fig. 7. Lab and airborne absorption depth analysis of chlorite (A-C) and ferric-hydroxide (D—F). C and F images show the correlation of the corresponding absorption depths and log of As ppm, the grey shaded area marks a 95 % confidence level. The field samples RSS1 and RSS23 were representative of mineralised samples and; RSS54 and RSS62 were representative of non-mineralised samples.

atmospheric and topographic effects (Richter and Schläpfer, 2010; Leifer et al., 2012; Vanonckelen et al., 2013). The VIS and NIR regions are further affected by the strong absorption of chlorophyll in vegetation (Haboudane et al., 2008; Moses et al., 2012), and potentially by the "exposed soil fraction".

4.3. Band selection and spectral correlations

The airborne dataset was analysed through RFE to subset spectral bands with the largest contribution to the targeted As concentration (Fig. 8A). The important bands are scattered throughout the spectrum, while many bands are selected from the SWIR. This can be due to the decreasing co-linearity of the input bands located further apart from each other, and/or due to less reflectance interference from chlorophyll in partial vegetation fraction cover. To further validate the bands selected by the RFE model, a Pearson-type correlation analysis between the laboratory-based reflectance spectra and As concentration represented by the pXRF counts at 10.54 keV from the 63 field samples was performed. Wavelengths that showed >0.2 coefficient that corresponds well with the expected absorption feature indicating chlorite-bearing rocks between 2240 and 2360 nm depending on the concentration of Fe and Mg (Neal et al., 2018; Cloutier et al., 2021) (Fig. 8B). The atmospheric water absorption bands ~1200 nm, 1450 nm and 1950 nm were discarded from the final spectral subset. A resultant set of 85 bands were selected which coincided with both the correlation analysis and the RFE output bands were then used for the rest of the workflow. The corresponding wavelengths of the 85 bands are provided in Supplementary Data (Table S2). The selected 85 bands still possess information regarding lithology, including mineralisation, topography, shadow and atmospheric effects and sensor noise. OTVCA was run to maximise spatially coherent variance in the input spectral data. Out of the first 10 components, 2 components were discarded which only consisted of sensor noise and scene boundaries (6th and 9th component) as analysed through visual interpretation (Fig. S2 in Supplementary data). The remaining 8 components were used to create potential zonation of As anomalies through image classification using a random forest classifier.

4.4. Indirect mineralisation mapping and classification

The training data contains 87,97 and 123 observations from high (>100 ppm), medium (20–100 ppm), and low (<20 ppm) As concentration zones respectively (Fig. S4). The overall accuracy of the classification is 0.58 (Table 3). The confusion matrix shows an ample number of misclassifications, among all three classes. A significant percentage of the misclassification was accountable to topographical and varying soil exposure fraction which was mixed in the training data as well. The highest class-wise accuracy is for the low concentration As class, which is 72 % and 66 % for producer's accuracy and user's accuracy (Table 4). This class has made up most of the study area, totalling a 9.2 km^2. On the other hand, the lowest accuracy is reported for the high concentration As class, presumed to be related to underlying mineralisation. The total area classified under high As concentration zone was 1.84 km^2 (Fig. 9).

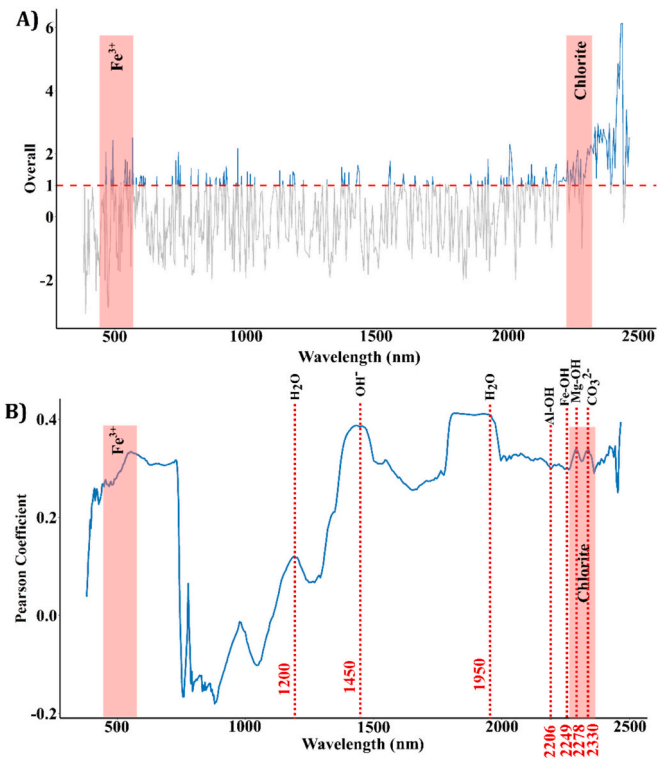

Fig. 8. The graphs illustrate A) the overall importance across the airborne hyperspectral data as an output from the RFE band selection method and B) the correlation across the laboratory-based hyperspectral data to the target As concentration. The highlighted red regions are the spectral ranges used in the "direct mapping" workflow. (For interpretation of the references to colour in this figure legend, the reader is referred to the web version of this article.)

Table 3
Error matrix of the random forest image classification using the independent validation data (columns) against the image classification results (row). The bold values show the correctly classified pixels.

	Reference			
Prediction	High	Medium	Low	Total
High	**42**	25	16	83
Med	24	**49**	19	92
Low	23	23	**88**	134
Sum	89	97	123	309

Table 4
Area statistics and Image classification accuracy by image classes.

Classes	User's Accuracy (%)	Producer's Accuracy (%)	F1 Accuracy (%)	Total area (pixel)	Total area (km^2)
High	51	48	50	460,820	1.84
Medium	53	51	52	756,242	3.02
Low	66	72	62	2,430,621	9.72

The F1 scores also being in the same order as the user's and producer's accuracy further prove consistency in the model performance (Dong et al., 2022; Liu et al., 2022).

The areas classified under "High" As concentration is based on the training data which contained As ppm concentrations at 307 field locations (Fig. 1). Although, the results show strong regional trends matching the geology. The surface manifestations of the arsenopyrite and scorodite-bearing rocks can also be impacted by surficial processes such as leaching and mainly represent ferric oxyhydroxide with different levels of adsorbed As (Fig. 5b).

5. Discussion

5.1. Arsenic as a pathfinder to gold and its spectral importance

Geochemically, As anomalies are an established and globally used pathfinder to gold deposits (Kovalev et al., 2011; Large et al., 2012; Blake et al., 2019). The gold mineralisation in Central Otago is mostly hosted by arsenopyrite in association with other sulphide minerals, such as chalcopyrite and stibnite (Craw and MacKenzie, 2007; Craw et al., 2007). With an increasing demand for gold, currently, there is more emphasis on exploring lower-grade gold deposits. The signal to these deeper-seated deposits is often shadowed by redistributed As halos due to supergene weathering and, leaching through groundwater circulation at a meter scale (Goldfarb et al., 2005; Blake et al., 2019; Jasiak et al., 2021). The lower green-schist facies zone at the RSSZ is less lithified and has more clay proportion thus enhancing the redistribution of As and increasing the amount of clay.

The supergene leaching facilitates enlarged alteration halos can pose a major drawback in mapping As anomalies to target gold at a regional scale. Other pathfinder elements to gold in the Otago RSSZ setting, such as Sb, can also be plausible alternatives because of their co-occurrence with As and Au (MacKenzie and Craw, 2007; Chakraborty et al., 2022). Elements such as Sb and As are released into the environment in a concurrent breakdown of stibnite and arsenopyrite respectively. Sb oxidises and can get precipitated nearer to the target gold-bearing host rock; on the contrary, As remains in solution and gets redistributed forming a larger As footprint (Ashley et al., 2003).

The mineralised samples exhibited a peak at 10.54 keV in the pXRF spectra signalling the presence of As in the mineralised field samples, whereas there was no such signal in the non-mineralised samples (Fig. 5). It is important to note that As-bearing rocks and minerals often have no unique absorption feature in the soil spectra in the VIS-SWIR region (Garcia-Sanchez and Alvarez-Ayuso, 2003; Shin et al., 2019; Tao et al., 2019), which can be directly used to infer its presence or absence. Any machine learning model based on hyperspectral data, therefore, associates As concentration with other physico-chemical features in soil, including soil moisture, vegetation type, soil exposure, and/or other mineral phases with unique absorption features which potentially can co-vary with As occurrence (Font et al., 2005; Hassan and Atkins, 2011; Wei et al., 2020; Shrestha et al., 2022). Although the greenschist facies rocks comprise minerals with characteristic absorption features (e.g., biotite, chlorite, carbonate, and smectite group of minerals), most of them cannot differentiate between mineralised and non-mineralised lower greenschist facies at RSSZ, This leaves depletion of chlorite the only feature to be used as a proxy for As using hyperspectral data.

The RFE band selection was run on the airborne hyperspectral data (predictor variable) against the raw pXRF counts at 10.54 keV (target variable) to select the most important bands contributing to this As variation (Fig. 5). However, the important bands in the SWIR range signal the consistent depletion of chlorite in the mineralised samples and the nearly ubiquitous presence of muscovite, and carbonate minerals (e.g., dolomite, ankerite), all of which have their significant absorption features in the SWIR (Fig. 8). This shift in mineralogy coincides with the depletion of As-bearing minerals and therefore represents an avenue to detect and quantify As with VNIR-SWIR hyperspectral data. Furthermore, the important bands in the VNIR region are attributed to the comparative abundance of ferric hydroxide-bearing minerals in the mineralised schist and the varied vegetation cover in the zone (Fig. 10). The subtle changes and shifts in these absorption features in indirect correspondence to As concentration in the samples fits the vectoring signals to the characteristics of the mineralised schist.

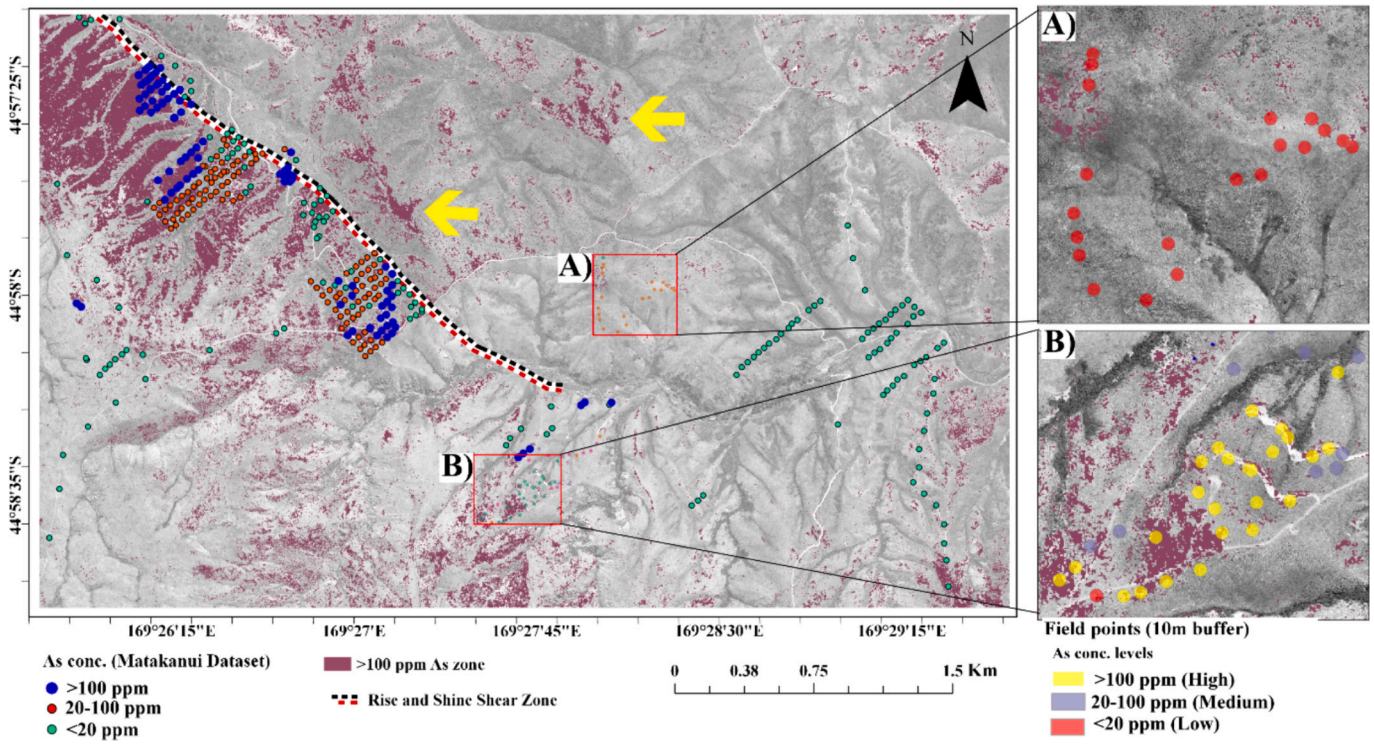

Fig. 9. Potential As zonation map showing "High" concentration As (magenta) spatially extrapolated through Random Forest classifier using known ground points. The image has been overlayed by all the ground points collected in the study and the Matakanui Gold Ltd. dataset. The insets show details of the non-mineralised (A) and the mineralised (B) sections respectively. The yellow arrows show misclassified patches of "High" As concentration in topographic valleys within the lower greenschist facies. (For interpretation of the references to colour in this figure legend, the reader is referred to the web version of this article.)

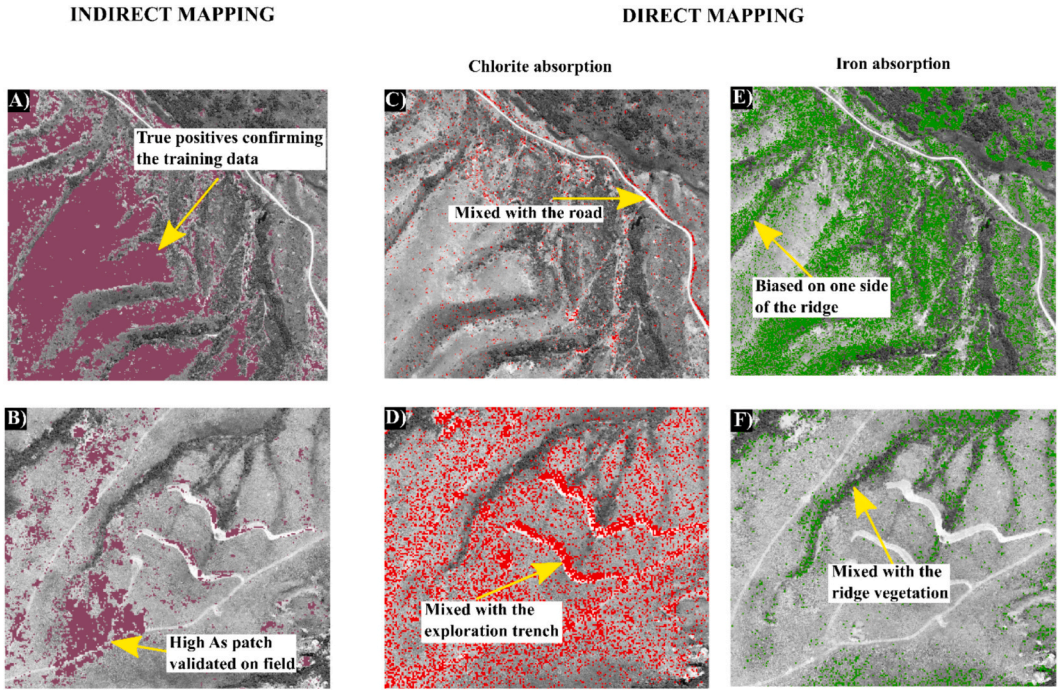

Fig. 10. A comparison showing the topographic effects on the As zonation using indirect method (A,B) and the direct mapping (C—F). Arrows indicate major on-surface differences between the two methods.

5.2. Band ratio vs multivariate data analysis for potential As zonation

Band ratio and direct mapping methods (e.g., Spectral Angle Mapper) are inherently limited to capture the variation of a single mineral group using its characteristic absorption feature caused by the chemical bonds and bulk compositions (Clark et al., 1990; van der Meer and Bakker, 1998; Clark, 1999; van Ruitenbeek et al., 2014; van der Meer, 2018; Shrestha et al., 2022). This can easily fall apart in a more

challenging environment where >90 % of the pixels are impure/mixed and have overlapping absorption ranges. This effect shows in the mapping results where the direct mapping gets often confused with undulated topography and the gullies whereas the indirect map results are much less impacted by topography (Fig. 10). In such a scenario, the interpretation of band ratio must require expert knowledge to be used to portray the underlying geology. Furthermore, the spectral signature of vegetation is stronger than most mineral signatures and can pose difficulty in analysing subtle shifts in mineral absorption when both have overlapping important wavelengths (Crippen and Blom, 1999).

High toxic levels of As leads to stunted plant growth and leaf colouration among others (Brooks, 1979; Farago, 2008) which are comparatively easier to detect using hyperspectral (Rodriguez-Gomez et al., 2023) and even multispectral data (Rencz, 1989). In ppm levels, when the effect of As is more at a molecular and chemical stage than apparent physical changes, integrated knowledge of chemical associations is thus preferred and here-in proposed as indirect zonation of As (Rathod et al., 2015; Shi et al., 2016; Shin et al., 2019; Chakraborty et al., 2022). Our study area offers a great test ground for lithological mapping and chemical zonation due to its highly variable soil exposures between 5 and 85 % over the known mineralisation. The proposed supervised classification approach can outperform any direct mapping methods due to its ability to tune the data through maximising correlation between target variables (pXRF measurement on the ground) and predictors (airborne hyperspectral data). The multivariate classification model can therefore pick up and relate with subtle spectral changes associated with near-surface mineralisation which cannot be associated with mapping absorption features of individual mineral phases alone. Thus, this approach not only can capture the underlying lithology but can also shed light on expected mineralisation levels using hyperspectral remote sensing.

5.3. *Connecting band selection and data transformation with the underlying geology*

Despite an extensive legacy of geological remote sensing, there are still considerable gaps in utilising remote sensing to mineral prospecting on complex terrains without or only partial soil/rock exposure and/or target minerals without a unique absorption feature. Our novel workflow combining RFE with OTVCA shows promise to tackle natural complexity and can provide a new tool to utilize in mineral prospecting and improved land-surface mapping. The iterative elimination process implemented in the RFE using a random forest base algorithm, can reduce dimensionality and deal with non-linear data (Su et al., 2017; Pullanagari et al., 2018; Demarchi et al., 2020). The RFE shows most bands across the VIS-SWIR spectrum with large amounts of bands form the SWIR corresponding to characteristic absorption bands of chlorite. Chlorite is geologically linked to As-concentration (depletion when As is present in the RSSZ setting) that the dimensionality reduction maximised in the input hyperspectral data to link with the most. Our mapping results benefits using OTVCA that can further enhance geological features by increasing the inherent spatial coherence. This is particularly useful in investigating geological systems, such as the gold mineralisation and lithological changes with high spatial autocorrelation (Warner and Shank, 1997). OTVCA is a spatially constrained data transformation technique that can maximise and generalise geological information explicitly. Consequently, the mineral prospecting classification results become more independent of the soil exposure fraction compared to non-transformed data and make it more generalised/smoothed.

6. Conclusion

Potential arsenic zonation to locate a concealed gold mineralisation is challenging using remote sensing. Firstly, As lacks any unique absorption feature in the VIS-SWIR spectral range, based on which most hyperspectral mapping techniques are tailored. Furthermore, As halo covers a large footprint than the target mineralisation due to leaching and transport by groundwater.

Anomalous pathfinder element concentrations can be used to define a proximal mineralisation halo and this is the key to mineral prospecting using biogeochemistry (Ashley and Craw, 2004; Hamisi et al., 2017; Laukamp et al., 2021a). The lateral extent of the proximal mineralisation halo related to orogenic gold mineralisation can vary from place to place. For example, in Yilgarn Craton in Western Australia, it extends over 200 m (Eilu and Groves, 2001); in Mali, West Africa, the characteristic ankerite and the sulphide anomalies extend up to 2 km (Lawrence et al., 2013); in the Minas Azules in Argentina it lies between 70 and 100 m (Rodríguez and Bierlein, 2003). The extent of the proximal mineralisation halo in the South Island, New Zealand varies from ~10 to ~100 m. Other than the magnitude of pathfinder element concentration defining mineralisation, the halo is also subjected to variation in lithology, surface topography and soil moisture. A combination of all these factors makes every setting unique and eventually poses a major drawback in generalising a remote sensing-based approach for mineral prospecting suitable to all settings. In this RSSZ settings, there is a strong correlation between the soil moisture and vegetation cover (e.g., plant associations) to the potential As anomalies indirectly vectoring to the gold mineralisation.

The topography and the varying soil exposure can add a significant percentage of information captured by hyperspectral imaging. Therefore, even if the characteristic absorption features exist for any target minerals, the lack of pure pixels can hamper wavelength-based approaches for image classification. Variable selection can help reducing bands, maximising relevant information and the prediction accuracy. The selected variables contain dominant target information and an essentially smaller percentage of background information. The band reduction via RFE and data transformation via OTVCA can simplify the information in the selected set of bands improving image classification accuracy. While mineral deposits are patchy geological systems the spatial correlation of the As halos to the gold mineralisation was maximised using OTVCA.

Compared to direct mapping using a single characteristic absorption feature or the information of a single band, the proposed indirect mapping returns improved results. This is an early attempt to use such an indirect workflow to map a target that is not “visible” to the sensor in any form. This study serves as a crucial step towards integrating the terrain, geological and spectral data into mineral prospecting. The study here is carried out from a geoscience perspective where the explainability of the rendered results from a geoscience perspective was majorly emphasised. However, future work in this study would be more addressed from a data science perspective to minimise the topographic effects further by using sub-pixel-based training and/or pixel-based membership value which would potentially improve the classification. Furthermore, this approach is not only confined to indirect mineral mapping but can also be expanded to map As toxicity levels in the environment. Thus, in the future, more generalised models for easier transferability across domains and study areas shall be attempted.

CRediT authorship contribution statement

Rupsa Chakraborty: Conceptualization, Data curation, Formal analysis, Methodology, Visualization, Writing – original draft. **Gabor Kereszturi:** Conceptualization, Funding acquisition, Project administration, Resources, Supervision, Writing – review & editing. **Reddy Pullanagari:** Data curation, Resources, Supervision, Writing – review & editing. **Dave Craw:** Supervision, Writing – review & editing. **Patricia Durance:** Supervision, Writing – review & editing. **Salman Ashraf:** Data curation, Supervision, Writing – review & editing.

Declaration of competing interest

The authors declare that they have no known competing financial

interests or personal relationships that could have appeared to influence the work reported in this paper.

Data availability

Data will be made available on request.

Acknowledgement

This study was supported by the Ministry of Business, Innovation and Employment (MBIE) Endeavour Fund – Smart Ideas: Assessing New Zealand's environmental and mineral indicators (contract number: MAUX1802). The authors are grateful for the support and access to exploration datasets carried out by Matakanui Gold Ltd. and Matakanui Station for the land access and for digging us out from the mud. The authors are also grateful to Dr. Daniel Coulthard and Massey University's Manawatu Imaging Centre for their assistance in the SEM-EDS analysis. The authors would also like to thank Dr. Mark Lawrence and GNS Lower Hutt for their assistance with the pXRF analysis.

Appendix A. Supplementary data

Supplementary data to this article can be found online at https://doi.org/10.1016/j.gexplo.2024.107510.

References

Abweny, M.S., van Ruitenbeek, F.J., de Smeth, B., Woldai, T., van der Meer, F.D., Cudahy, T., Zegers, T., Blom, J.-K., Thuss, B., 2016. Short-Wavelength Infrared (SWIR) spectroscopy of low-grade metamorphic volcanic rocks of the Pilbara Craton. J. Afr. Earth Sci. 117, 124–134.
Ashley, P., Craw, D., 2004. Structural controls on hydrothermal alteration and gold–antimony mineralisation in the Hillgrove area, NSW, Australia. Mineral. Deposita 39, 223–239.
Ashley, P., Craw, D., Graham, B.P., Chappell, D., 2003. Environmental mobility of antimony around mesothermal stibnite deposits, New South Wales, Australia and southern New Zealand. J. Geochem. Explor. 77, 1–14.
Belgiu, M., Drăguţ, L., 2016. Random forest in remote sensing: a review of applications and future directions. ISPRS J. Photogramm. Remote Sens. 114, 24–31.
Beyer, S.R., Kyser, K., Kotzer, T.G., Ansdell, K., Quirt, D., 2021. Exploration geochemistry of surficial media over the high-grade McArthur River uranium deposit, Saskatchewan, Canada. Can. Mineral. 59, 913–945.
Bishop, J.L., 2005. The visible and infrared spectral properties of jarosite and alunite. Am. Mineral. 90, 1100–1107.
Blake, F., Grant, K., MacKenzie, D., Scott, J., Craw, D., 2019. Surficial arsenic redistribution above gold-mineralised zones in East Otago, New Zealand. N. Z. J. Geol. Geophys. 1–15.
Boardman, J.W., Kruse, F.A., Green, R.O., 1995. Mapping Target Signatures Via Partial Unmixing of AVIRIS Data.
Breiman, L., 2001. Random Forests. Machine Learning, 45, pp. 5–32.
Brooks, R.R., 1979. Indicator plants for mineral prospecting - a critique. J. Geophys. Res. 12, 67–78.
Chakraborty, R., Kereszturi, G., Pullanagari, R., Durance, P., Ashraf, S., Anderson, C., 2022. Mineral prospecting from biogeochemical and geological information using hyperspectral remote sensing-Feasibility and challenges. J. Geochem. Explor. 106900.
Chauhan .N., P.K.P.S., Sinha, Rishitosh K., Jain, Nirmala, Murty, S.V.S., 2015. Hyperspectral remote sensing of planetary surfaces: an insight into composition of inner planets and samall bodies in the solar system. Curr. Sci. 108, 915–924.
Cheng, J.-H., Sun, D.-W., 2016. Partial Least Squares Regression (PLSR) applied to NIR and HSI spectral data modeling to predict chemical properties of fish muscle. Food Eng. Rev. 9, 36–49.
Christie, A., 2016. Mineral Deposits of New Zealand: Exploration and Research. Australasian Institute of Mining and Metallurgy.
Clark, R.N., 1999. Spectroscopy of Rocks and Minerals and Principles of Spectroscopy. Manual of Remote Sensing, Remote Sensing for the Earth Sciences.
Clark, R.N., King, T.V., Klejwa, M., Swayze, G.A., Vergo, N., 1990. High spectral resolution reflectance spectroscopy of minerals. J. Geophys. Res. 95.
Clark, R.N., Swayze, G., Boardman, J., Kruse, F., 1993. Comparison of Three Methods for Materials Identification and Mapping With Imaging Spectroscopy.
Clark, R.N., Swayze, G.A., Livo, K.E., Kokaly, R.F., Sutley, S.J., Dalton, J.B., McDougal, R. R., Gent, C.A., 2003. Imaging spectroscopy: Earth and planetary remote sensing with the USGS Tetracorder and expert systems. J. Geophys. Res. Planets 108.
Cloutier, J., Piercey, S.J., Huntington, J., 2021. Mineralogy, mineral chemistry and SWIR spectral reflectance of chlorite and white mica. Minerals 11, 471.
Cox, L., Mackenzie, D.J., Craw, D., Norris, R.J., Frew, R., 2006. Structure and geochemistry of the Rise & Shine Shear Zone mesothermal gold system, Otago Schist, New Zealand. N. Z. J. Geol. Geophys. 49, 429–442.
Craw, D., 1994. Contrasting alteration mineralogy at an unconformity beneath auriferous terrestrial sediments, central Otago, New Zealand. Sediment. Geol. 92, 17–30.
Craw, D., 2017. Placer gold and associated supergene mineralogy at Macraes Flat, East Otago, New Zealand. N. Z. J. Geol. Geophys. 60, 353–367.
Craw, D., Lilly, K., 2016. Gold nugget morphology and geochemical environments of nugget formation, southern New Zealand. Ore Geol. Rev. 79, 301–315.
Craw, D., MacKenzie, D., 2007. Disseminated Gold in Ankeritic Alteration Zones. Rise & Shine and Shotover, Otago Schist.
Craw, D., Mackenzie, D.J., Begbie, M., Norris, R.J., 2005. Late Metamorphic Structural Zones in the Otago Schist: Prospective Hosts for Gold Mineralisation. Realising New Zealand's mineral potential, NZ Minerals Conference, pp. 89–97.
Craw, D., MacKenzie, D., Pitcairn, I., Teagle, D., Norris, R., 2007. Geochemical signatures of mesothermal Au-mineralized late-metamorphic deformation zones, Otago Schist, New Zealand. J. Geochem. Explor. Environ. Anal. 7, 225–232.
Craw, D., MacKenzie, D., Grieve, P., 2015. Supergene gold mobility in orogenic gold deposits, Otago Schist, New Zealand. N. Z. J. Geol. Geophys. 58, 123–136.
Crippen, R., Blom, R., 1999. Unveiling the Lithology of Vegetated Terrains in Remotely Sensed Imagery.
Cudby, J., Scott, J.M., Craw, D., Hesson, M., Rufaut, C., 2021. Surficial redistribution of gold and arsenic from the Rise and Shine Shear Zone, Otago, New Zealand. N. Z. J. Geol. Geophys. 1–15.
Dalm, M., Buxton, M., van Ruitenbeek, F., 2017. Discriminating ore and waste in a porphyry copper deposit using short-wavelength infrared (SWIR) hyperspectral imagery. Miner. Eng. 105, 10–18.
Demarchi, L., Kania, A., Ciężkowski, W., Piórkowski, H., Oświecimska-Piasko, Z., Chormański, J., 2020. Recursive feature elimination and random forest classification of natura 2000 grasslands in lowland river valleys of Poland based on airborne hyperspectral and LiDAR data fusion. Remote Sens. 12, 1842.
Dong, Y., Fan, L., Zhao, J., Huang, S., Geiß, C., Wang, L., Taubenböck, H., 2022. Mapping of small water bodies with integrated spatial information for time series images of optical remote sensing. J. Hydrol. 614, 128580.
Durance, P., Jowitt, S., Bush, K., 2014. An assessment of portable X-ray fluorescence spectroscopy in mineral exploration, Kurnalpi Terrane, Eastern Goldfields Superterrane, Western Australia. Appl. Earth Sci. 123, 150–163.
Eilu, P., Groves, D., 2001. Primary alteration and geochemical dispersion haloes of Archaean orogenic gold deposits in the Yilgarn Craton: the pre-weathering scenario. In: Geochemistry: Exploration, Environment, Analysis, 1, pp. 183–200.
Farago, M.E., 2008. Plants and the Chemical Elements: Biochemistry, Uptake, Tolerance and Toxicity. John Wiley & Sons.
Fauvel, M., Tarabalka, Y., Benediktsson, J.A., Chanussot, J., Tilton, J.C., 2012. Advances in spectral-spatial classification of hyperspectral images. Proc. IEEE 101, 652–675.
Font, R., Vélez, D., Río-Celestino, M.D., De Haro-Bailón, A., Montoro, R., 2005. Screening inorganic arsenic in rice by visible and near-infrared spectroscopy. Microchim. Acta 151, 231–239.
Garcia-Sanchez, A., Alvarez-Ayuso, E., 2003. Arsenic in soils and waters and its relation to geology and mining activities (Salamanca Province, Spain). J. Geochem. Explor. 80 (1), 69–79.
Ghamisi, P., Plaza, J., Chen, Y., Li, J., Plaza, A.J., 2017a. Advanced Spectral Classifiers for Hyperspectral Images: a review. IEEE Geosci. Remot. Sens. Mag. 5, 8–32.
Ghamisi, P., Yokoya, N., Li, J., Liao, W., Liu, S., Plaza, J., Rasti, B., Plaza, A., 2017b. Advances in hyperspectral image and signal processing: a comprehensive overview of the state of the art. IEEE Geosci. Remot. Sens. Mag. 5, 37–78.
Gislason, P.O., Benediktsson, J.A., Sveinsson, J.R., 2006. Random forests for land cover classification. Pattern Recogn. Lett. 27, 294–300.
Goldfarb, R., Baker, T., Dube, B., Groves, D.I., Hart, C.J., Gosselin, P., 2005. Distribution, Character and Genesis of Gold Deposits in Metamorphic Terranes. Society of Economic Geologists.
Guyon, I., Elisseeff, A., 2003. An introduction to variable and feature selection. J. Mach. Learn. Res. 3, 1157–1182.
Haboudane, D., Tremblay, N., Miller, J.R., Vigneault, P., 2008. Remote estimation of crop chlorophyll content using spectral indices derived from hyperspectral data. IEEE Trans. Geosci. Remote Sens. 46, 423–437.
Hamisi, J., MacKenzie, D., Pitcairn, I., Blakemore, H., Zack, T., Craw, D., 2017. Hydrothermal footprint of the Birthday Reef, Reefton goldfield, New Zealand. N. Z. J. Geol. Geophys. 60, 59–72.
Han, H., Guo, X., Yu, H., 2016. Variable selection using mean decrease accuracy and mean decrease gini based on random forest, 2016 7th ieee international conference on software engineering and service science (icsess). IEEE 219–224.
Hassan, M.M., Atkins, P.J., 2011. Application of geostatistics with indicator kriging for analyzing spatial variability of groundwater arsenic concentrations in Southwest Bangladesh. J. Environ. Sci. Health A 46 (11), 1185–1196.
Hengl, T., Nussbaum, M., Wright, M., Heuvelink, G., Gräler, B., 2018. Random forest as a generic framework for predictive modeling of spatial and spatio-temporal variables. PeerJ 6, e5518.
Hunt, G.R., 1982. Spectroscopic Properties of Rocks and Minerals. Handbook of Physical Properties of Rocks.
Jasiak, I., Wiklund, J., Leclerc, E., Telford, J., Couture, R., Venkiteswaran, J., Hall, R., Wolfe, B., 2021. Evaluating spatiotemporal patterns of arsenic, antimony, and lead deposition from legacy gold mine emissions using lake sediment records. Appl. Geochem. 105053.
Kereszturi, G., Schaefer, L.N., Schleiffarth, W.K., Procter, J., Pullanagari, R.R., Mead, S., Kennedy, B., 2018. Integrating airborne hyperspectral imagery and LiDAR for volcano mapping and monitoring through image classification. Int. J. Appl. Earth Obs. Geoinf. 73, 323–339.

Kereszturi, G., Schaefer, L.N., Miller, C., Mead, S., 2020. Hydrothermal alteration on composite volcanoes–mineralogy, hyperspectral imaging and aeromagnetic study of Mt Ruapehu, New Zealand. Geochem. Geophys. Geosyst. e2020GC009270.
Kovalev, K.R., Kalinin, Y.A., Naumov, E.A., Kolesnikova, M.K., Korolyuk, V.N., 2011. Gold-bearing arsenopyrite in eastern Kazakhstan gold-sulfide deposits. Russ. Geol. Geophys. 52, 178–192.
Kriesel, J.M., Gat, N., Bernacki, B.E., Erikson, R.L., Cannon, B.D., Myers, T.L., Bledt, C. M., Harrington, J.A., 2011. Hollow core fiber optics for mid-wave and long-wave infrared spectroscopy, Chemical, Biological, Radiological, Nuclear, and Explosives (CBRNE) Sensing XII. Int. Soc. Opt. Photon. 80180V.
Kruse, F.A., 1998. Advances in Hyperspectral Remote Sensing for Geologic Mapping and Exploration.
Kruse, F.A., 2007. Identification and mapping of minerals in drill core using hyperspectral image analysis of infrared reflectance spectra. Int. J. Remote Sens. 17, 1623–1632.
Kruse, F.A., Boardman, J.W., Huntington, J.F., 2003. Comparison of airborne hyperspectral data and eo-1 hyperion for mineral mapping. IEEE Trans. Geosci. Remote Sens. 41, 1388–1400.
Kruse, F.A., Bedell, R.L., Taranik, J.V., Peppin, W.A., Weatherbee, O., Calvin, W.M., 2012. Mapping alteration minerals at prospect, outcrop and drill core scales using imaging spectrometry. Int. J. Remote Sens. 33, 1780–1798.
Kursa, M.B., Jankowski, A., Rudnicki, W.R., 2010. Boruta–a system for feature selection. Fundament. Inform. 101, 271–285.
Kusuma, K., Sebastian, N., Murty, S., 2012. Geochemical and mineralogical analysis of Gruithuisen region on Moon using M3 and DIVINER images. Planet. Space Sci. 67, 46–56.
Large, R., Thomas, H., Craw, D., Henne, A., Henderson, S., 2012. Diagenetic pyrite as a source for metals in orogenic gold deposits, Otago Schist, New Zealand. N. Z. J. Geol. Geophys. 55, 137–149.
Laukamp, C., LeGras, M., Lau, I.C., 2021a. Hyperspectral proximal sensing instruments and their applications for exploration through cover. Port. Spectrosc. Spectromet. 401–422.
Laukamp, C., Rodger, A., LeGras, M., Lampinen, H., Lau, I.C., Pejcic, B., Stromberg, J., Francis, N., Ramanaidou, E., 2021b. Mineral physicochemistry underlying feature-based extraction of mineral abundance and composition from shortwave, mid and thermal infrared reflectance spectra. Minerals 11, 347.
Lawrence, D.M., Treloar, P.J., Rankin, A.H., Harbidge, P., Holliday, J., 2013. The geology and mineralogy of the Loulo mining district, Mali, West Africa: evidence for two distinct styles of orogenic gold mineralization. Econ. Geol. 108, 199–227.
Leifer, I., Tratt, D.M., Realmuto, V.J., Gerilowski, K., Burrows, J.P., 2012. Remote sensing atmospheric trace gases with infrared imaging spectroscopy. EOS Trans. Am. Geophys. Union 93, 525.
Liu, C., Frazier, P., Kumar, L., 2007. Comparative assessment of the measures of thematic classification accuracy. Remote Sens. Environ. 107, 606–616.
Liu, X., Liu, X., Wang, Z., Huang, G., Shu, R., 2022. Classification of laser footprint based on random forest in mountainous area using GLAS full-waveform features. IEEE J. Select. Top. Appl. Earth Observ. Remot. Sens. 15, 2284–2297.
Lotfollahi, M., Tran, N., Berisha, S., Gajjela, C., Han, Z., Mayerich, D., Reddy, R., 2020. Adaptive Compressive Sampling for Mid-infrared Spectroscopic Imaging. arXiv Preprint arXiv:2008.00566.
MacKenzie, D.J., Craw, D., 2007. Contrasting hydrothermal alteration mineralogy and gechemistry in the auriferous Rise & Shine Shear Zone, Otago New Zealand. N. Z. J. Geol. Geophys. 50, 67–69.
MacKenzie, D.J., Corner, N.G., Craw, D., 2006. Rise and Shine Shear Zone, Central Otago. Geology Exploration of New Zealand Mineral Deposits.
Martin, A., Turnbull, R., Rattenbury, M., Cohen, D., Hoogewerff, J., Rogers, K., Baisden, W., Christie, A., 2016. The regional geochemical baseline soil survey of southern New Zealand: Design and initial interpretation. J. Geochem. Explor. 167, 70–82.
Martin, A., Allibone, A., Blakemore, H., Blundell, C., Cox, S., Craw, D., Doyle, S., MacKenzie, D., Mortimer, N., Rattenbury, M., 2018. A New 1: 50 000 Scale Map and GIS Dataset of the Hyde-Macraes Shear Zone.
van der Meer, F.D., 2001. Spectral Matching using pixel cross-correlograms for the analysis of LANDSAT TM data. JAG 3.
van der Meer, F.D., 2018. Near-infrared laboratory spectroscopy of mineral chemistry_ a review. Int. J. Appl. Earth Obs. Geoinf. 65, 71–78.
van der Meer, F.D., Bakker, W., 1997. Cross Correlogram Spectral Matching: Application to Surface Mineralogical Mapping by Using AVIRIS Data from Cuprite. Nevada, Remote Sensing Environment.
van der Meer, F.D., Bakker, W., 1998. Validated surface mineralogy from high-spectral resolution remote sensing: a review and a novel approach applied to gold exploration using AVIRIS data. Surf. Mineral. High-resolut. Remot. Sens. 10, 112–119.
van der Meer, F., Kopačková, V., Koucká, L., van der Werff, H.M., van Ruitenbeek, F.J., Bakker, W.H., 2018a. Wavelength feature mapping as a proxy to mineral chemistry for investigating geologic systems: an example from the Rodalquilar epithermal system. Int. J. Appl. Earth Obs. Geoinf. 64, 237–248.
van der Meer, F., Kopačková, V., Koucká, L., van der Werff, H.M.A., van Ruitenbeek, F.J. A., Bakker, W.H., 2018b. Wavelength feature mapping as a proxy to mineral chemistry for investigating geologic systems: an example from the Rodalquilar epithermal system. Int. J. Appl. Earth Obs. Geoinf. 64, 237–248.
Mielke, C., Boesche, N., Rogass, C., Kaufmann, H., Gauert, C., de Wit, M., 2014. Spaceborne mine waste mineralogy monitoring in South Africa, applications for modern push-broom missions: Hyperion/OLI and EnMAP/Sentinel-2. Remote Sens. 6, 6790–6816.
Mortensen, J.K., Craw, D., MacKenzie, D.J., Gabites, J.E., Ulrich, T., 2010. Age and origin of orogenic gold mineralization in the Otago Schist Belt, South Island, New Zealand: constraints from lead isotope and 40Ar/39Ar dating studies. Econ. Geol. 105, 77–793.
Mortimer, N., 2000. Metamorphic discontinuities in orogenic belts: example of the garnet-biotite-albite zone in the Otago Schist, New Zealand. Int. J. Earth Sci. 89, 295–306.
Moses, W.J., Gitelson, A.A., Perk, R.L., Gurlin, D., Rundquist, D.C., Leavitt, B.C., Barrow, T.M., Brakhage, P., 2012. Estimation of chlorophyll-a concentration in turbid productive waters using airborne hyperspectral data. Water Res. 46, 993–1004.
Naik, P., Dalponte, M., Bruzzone, L., 2021. Prediction of forest aboveground biomass using multitemporal multispectral remote sensing data. Remote Sens. 13, 1282.
Neal, L.C., Wilkinson, J.J., Mason, P.J., Chang, Z., 2018. Spectral characteristics of propylitic alteration minerals as a vectoring tool for porphyry copper deposits. J. Geochem. Explor. 184, 179–198.
Notesco, G., Kopačková, V., Rojík, P., Schwartz, G., Livne, I., Ben Dor, E., 2014a. Mineral classification of land surface using multispectral LWIR and hyperspectral SWIR remote-sensing data. A case study over the Sokolov lignite open-pit mines, the Czech Republic. Remote Sens. 6, 7005–7025.
Notesco, G., Kopačková, V., Rojík, P., Schwartz, G., Livne, I., Dor, E., 2014b. Mineral classification of land surface using multispectral LWIR and hyperspectral SWIR remote-sensing data. A case study over the Sokolov Lignite Open-Pit Mines, the Czech Republic. Remote Sens. 6, 7005–7025.
Paul, D., Bair, E., Hastie, T., Tibshirani, R., 2008. "Preconditioning" for feature selection and regression in high-dimensional problems. Ann. Stat. 36, 1595–1618.
Pour, A.B., Hashim, M., 2011. Identification of hydrothermal alteration minerals for exploring of porphyry copper deposit using ASTER data, SE Iran. J. Asian Earth Sci. 42, 1309–1323.
Pullanagari, R., Kereszturi, G., Yule, I.J., Ghamisi, P., 2017a. Assessing the performance of multiple spectral–spatial features of a hyperspectral image for classification of urban land cover classes using support vector machines and artificial neural network. J. Appl. Remote. Sens. 11.
Pullanagari, R.R., Kereszturi, G., Yule, I., 2017b. Quantification of dead vegetation fraction in mixed pastures using AisaFENIX imaging spectroscopy data. Int. J. Appl. Earth Obs. Geoinf. 58, 26–35.
Pullanagari, R., Kereszturi, G., Yule, I., 2018. Integrating airborne hyperspectral, topographic, and soil data for estimating pasture quality using recursive feature elimination with random forest regression. Remote Sens. 10.
Rasti, B., Ulfarsson, M.O., Sveinsson, J.R., 2016. Hyperspectral feature extraction using total variation component analysis. IEEE Trans. Geosci. Remote Sens. 54, 6976–6985.
Rasti, B., Hong, D., Hang, R., Ghamisi, P., Kang, X., Chanussot, J., Benediktsson, J.A., 2020. Feature extraction for hyperspectral imagery: the evolution from shallow to deep: overview and toolbox. IEEE Geosci. Remot. Sens. Mag. 8, 60–88.
Rathod, P.H., Brackhage, C., Van der Meer, F.D., Müller, I., Noomen, M.F., Rossiter, D.G., Dudel, G.E., 2015. Spectral changes in the leaves of barley plant due to phytoremediation of metals—results from a pot study. Eur. J. Remot. Sens. 48, 283–302.
Rathod, P.H., Brackhage, C., Müller, I., Van der Meer, F.D., Noomen, M.F., 2018. Assessing metal-induced changes in the visible and near-infrared spectral reflectance of leaves: a pot study with sunflower (Helianthus annuus L.). J. Indian Soc. Remot. Sens. 46, 1925–1937.
Rencz .G.P., A.N.W., 1989. Biogeochemistry and LANDSAT TM data: application to gold exploration in northern New Brunswick. J. Geochem. Explor. 271–284.
Richter, R., Schläpfer, D., 2010. Geo-atmospheric processing of airborne imaging spectrometry data. Part 2: Atmospheric/topographic correction. Int. J. Remote Sens. 23, 2631–2649.
Rodríguez, G.A., Bierlein, F.P., 2003. Nature and dimension of orogenic gold-related hydrothermal alteration at Minas Azules, NW Argentina, Society for Geology Applied to Mineral Deposits Biennial Meeting 2003. Millpress Sci. 807–810.
Rodriguez-Gomez, C., Kereszturi, G., Reeves, R., Rae, A., Pullanagari, R., Jeyakumar, P., Procter, J., 2021. Lithological mapping of Waiotapu Geothermal Field (New Zealand) using hyperspectral and thermal remote sensing and ground exploration techniques. Geothermics 96, 102195.
Rodriguez-Gomez, C., Kereszturi, G., Whitehead, M., Reeves, R., Rae, A., Pullanagari, R., 2023. Point pattern analysis of thermal anomalies in geothermal fields and its use for inferring shallow hydrological processes. Geothermics 110, 102664.
van Ruitenbeek, F.J.A., Cudahy, T., Hale, M., van der Meer, F.D., 2005. Tracing fluid pathways in fossil hydrothermal systems with near-infrared spectroscopy. Geology 33.
van Ruitenbeek, F.J.A., Bakker, W.H., van der Werff, H.M.A., Zegers, T.E., Oosthoek, J.H. P., Omer, Z.A., Marsh, S.H., van der Meer, F.D., 2014. Mapping the wavelength position of deepest absorption features to explore mineral diversity in hyperspectral images. Planet. Space Sci. 101, 108–117.
Sabins, F.F., 1999. Remote sensing for mineral exploration. Ore Geol. Rev. 14, 157–183.
Shi, T., Wang, J., Chen, Y., Wu, G., 2016. Improving the prediction of arsenic contents in agricultural soils by combining the reflectance spectroscopy of soils and rice plants. Int. J. Appl. Earth Obs. Geoinf. 52, 95–103.
Shin, Yu, Wang, Kim, Koh, 2019. Investigation of spectral variation of pine needles as an indicator of arsenic content in soils. Minerals 9.
Shrestha, G., Calvelo-Pereira, R., Roudier, P., Martin, A., Turnbull, R., Kereszturi, G., Jeyakumar, P., Anderson, C., 2022. Quantification of multiple soil trace elements by combining portable X-ray fluorescence and reflectance spectroscopy. Geoderma 409, 115649.

Simpson, M.P., Christie, A.B., 2019. Hydrothermal alteration mineralogical footprints for New Zealand epithermal Au-Ag deposits. N. Z. J. Geol. Geophys. 62, 483–512.
Su, J., Yi, D., Liu, C., Guo, L., Chen, W.-H., 2017. Dimension reduction aided hyperspectral image classification with a small-sized training dataset: experimental comparisons. Sensors 17, 2726.
Swayze, G.A., Clark, R.N., Goetz, A.F., Livo, K.E., Breit, G.N., Kruse, F.A., Sutley, S.J., Snee, L.W., Lowers, H.A., Post, J.L., 2014. Mapping advanced argillic alteration at Cuprite, Nevada, using imaging spectroscopy. Econ. Geol. 109, 1179–1221.
Tao, C., Wang, Y., Cui, W., Zou, B., Zou, Z., Tu, Y., 2019. A transferable spectroscopic diagnosis model for predicting arsenic contamination in soil. Sci. Total Environ. 669, 964–972.
Tripathi, P., Garg, R., 2021. Integration of Raman, emission, and reflectance spectroscopy for earth and lunar mineralogy. J. Appl. Remote. Sens. 15, 036502.
Ullah, S., Schlerf, M., Skidmore, A.K., Hecker, C., 2012. Identifying plant species using mid-wave infrared (2.5–6 μm) and thermal infrared (8–14 μm) emissivity spectra. Remote Sens. Environ. 118, 95–102.
Vanonckelen, S., Lhermitte, S., Van Rompaey, A., 2013. The effect of atmospheric and topographic correction methods on land cover classification accuracy. Int. J. Appl. Earth Obs. Geoinf. 24, 9–21.
Warner, T.A., Shank, M.C., 1997. Spatial autocorrelation analysis of hyperspectral imagery for feature selection. Remote Sens. Environ. 60, 58–70.
Wei, L., Pu, H., Wang, Z., Yuan, Z., Yan, X., Cao, L., 2020. Estimation of Soil Arsenic Content with Hyperspectral Remote Sensing. Sensors (Basel) 20.
Wu, J.-z., Yan, W.-d., Ni, W.-p., Bian, H., 2013. Feature extraction for hyperspectral data based on MNF and singular value decomposition, 2013 IEEE International Geoscience and Remote Sensing Symposium-IGARSS. IEEE 1430–1433.
Zhou, Q., Zhou, H., Zhou, Q., Yang, F., Luo, L., 2014. Structure damage detection based on random forest recursive feature elimination. Mech. Syst. Signal Process. 46, 82–90.
Zou, H., 2006. The adaptive lasso and its oracle properties. J. Am. Stat. Assoc. 101, 1418–1429.